

Strong-field control landscapes of coherent electronic excitation

Tim Bayer, Matthias Wollenhaupt and Thomas Baumert

Universität Kassel, Institut für Physik und CINSaT, Heinrich-Plett-Str 40, D-34132 Kassel, Germany

E-mail: wollenha@physik.uni-kassel.de


Received 5 October 2007, in final form 19 December 2007

Published 25 March 2008

Online at stacks.iop.org/JPhysB/41/074007

Abstract

We report on physical mechanisms behind resonant strong-field coherent control. To this end, we study multi-photon ionization of potassium atoms using intense shaped femtosecond laser pulses. The measured photoelectron spectra are discussed in terms of selective population of dressed states (SPODS). A physically motivated pulse parameterization is introduced which opens up two-dimensional parameter spaces comprising pulse sequences as well as chirped pulses. The control topologies of these subspaces are mapped out experimentally and are presented in the form of strong-field control landscapes (SFCLs). In the SFCLs, complementary realizations of SPODS via photon locking and rapid adiabatic passage are observed. Moreover, the combined effect, termed Multi-RAP, arises when both mechanisms are at play simultaneously. In order to better understand the performance of adaptive optimization procedures, we experimentally study their capability to find optimal solutions on a given parameter space. The evolution of different optimization procedures is visualized by means of control trajectories on the surface of the measured SFCL.

 This article features online multimedia enhancements

1. Introduction

The development and rapid progress in the ultrashort laser pulse-shaping technology [1, 2] provides the ability to generate pulses of unprecedented complexity. On the one hand, these pulses have opened entirely new perspectives to manipulate light–matter interactions [3, 4] at a high level of sophistication with applications ranging from basic research, nonlinear optics, materials processing, quantum computing to coherent control of chemical reactions. On the other hand, these complex pulses create new challenges in understanding the physical processes of the complex light-induced dynamics. Although concepts for understanding perturbative control scenarios have been devised [3, 4], non-perturbative control by intense shaped laser fields is still largely unexplored. These laser pulses open new pathways by modifying the energies of the involved quantum states up to hundreds of meV via the optical Stark effect [5]. These novel pathways on the light-induced potentials open new reaction channels which are inaccessible in weak laser fields. Experimental demonstrations of non-resonant strong-field control comprise the observation of non-Franck–Condon transitions in bound wave packet motion [6] and control of the branching ratio

in a dissociation reaction [7]. Both observations highlight the importance to analyse strong-field-induced dynamics in terms of light-induced potentials [8, 9]. A very efficient way to manipulate the energy of the light-induced potentials and hence an extended degree of control is provided by the use of shaped *resonant* laser pulses. Since the resonant control pathways will always dominate the controlled dynamics, resonant control scenarios will be more and more important as shorter and shorter pulses with ultrabroad spectra become available.

Figure 1 shows the general picture of resonant strong-field control. In this scenario, the control is exerted via the intermediate resonant state $|r\rangle$. In general, strong laser fields give rise to an energy splitting of the resonant state into two (so-called dressed) states in the order of $\hbar\Omega$, where Ω describes the Rabi frequency. The decisive step in switching among different final electronic states is realized by the manipulation of dressed state energies and dressed state populations. By suitable phase shaping of the driving laser field, it is possible to populate one of these two (dressed) states [10], i.e. to realize selective population of dressed states (SPODS). Effectively, the population of a single dressed state amounts to a controlled energy shift of the resonant state into a desired direction as

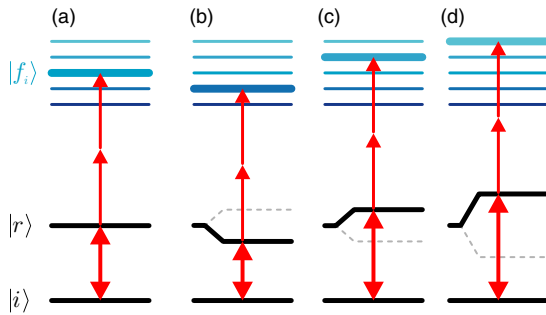


Figure 1. Quantum control of multi-photon processes via intermediate resonant states: (a) shaped resonant laser pulses steer the population from the initial state $|i\rangle$ via an intermediate resonant state $|r\rangle$ to a single target state $|f\rangle$ within a manifold of final states $|f_i\rangle$; (b) and (c) selectivity in the population transfer is obtained by manipulating the energy and population of the dressed states; (d) shows tunability among the target states.

illustrated in figures 1(b) and (c) for the lower and upper dressed states, respectively. By the variation of the laser intensity the energy splitting can be controlled, and thus a particular target state among the manifold of final states is addressed (cf figure 1(d)) providing tunability.

A combination of pulse-shaping techniques with adaptive feedback learning algorithms [11–15] allows us to optimize virtually any conceivable observable as reviewed, for example, in [2, 16]. The adaptive optimization algorithms involved generally operate on the extremely large space of available pulse shapes. All imaginable pulse shapes constitute the *control space* which has an infinite number of dimensions defined by independent parameters to describe the pulse shape. From the theoretical point of view, the interaction of the shaped pulse with a given quantum system provides a functional that maps the control space onto a specific real-valued control observable. This mapping is generally referred to as the quantum control landscape introduced by Rabitz *et al* [17]. Theoretical studies on the topology of quantum control landscapes [17, 18] reveal that for controllable quantum systems the global optimum is always attainable. Moreover, adaptive search strategies would benefit from gentle slopes with no trapping suboptimal extrema and a remarkable robustness of the optimal solution. However, experimental constraints, such as limited pulse intensities, the available bandwidth of the laser system and a fixed laser polarization, inherently confines the laboratory search to a lower dimensional subset of the control space which is generally termed *search space*. Approaches to extend the search space by the use of polarization-shaping techniques have been reported recently [19, 20]. The mapping of the search space gives a section of the quantum control landscape and, hence, might exhibit a more complex topology. In particular, the occurrence of saddle points or suboptimal local extrema can no longer be ruled out and search pathways of adaptive optimization algorithms across the landscape will in general be tortuous and may encounter multiple local extrema. In addition, measurement conditions such as noise or random orientation of molecules in the sample might obstruct the passage to existing optimal extrema. The latter issue was

recently addressed by the use of alignment pulses prior to the experiment [21, 22] and the investigation of adaptive alignment strategies [23, 24]. As a consequence, there is no guarantee to reach the global optimum under experimentally constrained conditions.

The localization of optimal solutions is further complicated by the fact that the search space is still dauntingly high dimensional. In order to appropriately reduce the number of search space dimensions, different approaches to facilitate laboratory searches have been proposed. A basic approach is the reduction of sampling points of the modulation function in the pulse shaper—for instance by pixel binning [25]. In this approach, artificial phase jumps are introduced by undersampling simple continuous phase functions. Another approach utilizes the set of pulse shapes obtained during an optimization procedure to extract relevant degrees of freedom by statistical analysis [26–28]. Pulse parameterization, i.e. the use of certain basis functions, is a powerful tool to generate shaped pulses in a search space of manageable dimension. Polynomial or sinusoidal phase functions which produce reasonably smooth pulse shapes have been used to investigate the topology of parameterized search spaces [29–31]. The use of binary phase masks was demonstrated as a convenient tool for search space mapping [32]. Despite the simplicity of the spectral phase in this approach, the temporal pulse shape is generally highly complex, making a detailed analysis of physical mechanisms difficult. An automated approach to extract mechanistic information from parameterized search space mapping by basis transformations was investigated in [33, 34].

However, the interpretation of adaptively determined pulse shapes is still a challenge. In order to shine light into strong-field-induced quantum dynamics, we devise control parameters motivated by insights into the physical mechanisms at play. In our experiments, the control topology of these parameter spaces is mapped out systematically and presented in the form of strong-field control landscapes (SFCLs). Analysis of the measured SFCLs yields maps of the underlying physical mechanisms. These results are used to examine the performance of an adaptive optimization procedure on a landscape surface found in the experiment. With the help of control trajectories (CTs) derived from the pulse individual distributions of different generations during the optimization, the evolution of the optimization algorithm on the measured landscape is investigated. Our goal is to generalize our findings in order to devise a set of adequately chosen robust parameters suitable to study resonant strong-field quantum control scenarios.

This paper is organized as follows: first, we introduce the physical system under study in section 2. In section 3, we describe our experimental setup and the strategy behind search space mapping. In section 4, the experimentally obtained SFCLs are presented and analysed in terms of control by SPODS (section 4.1). Furthermore, results from an adaptive optimization procedure on one of the parameter spaces are visualized by measured CTs on the corresponding SFCL (section 4.2). Section 5 ends this paper with a brief summary and conclusions.

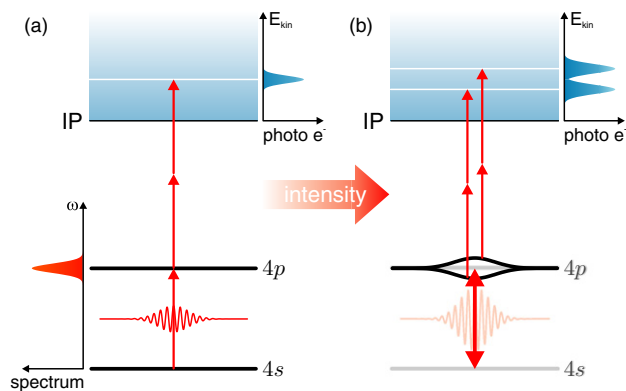


Figure 2. Excitation and ionization scheme of potassium atoms exposed to a resonant unshaped laser pulse: (a) weak-field excitation triggers a 1+2 REMPI process giving rise to a single peak in the photoelectron spectrum; (b) in the strong-field regime, the peak splits up into the Autler–Townes doublet due to Rabi cycling (bilateral photon arrow) among the bare states $4s$ and $4p$. In the dressed state picture, this splitting results from a splitting of dressed state eigenenergies (bold) proportional to the Rabi frequency.

2. The physical system

The experimental implementation of the control scheme introduced in figure 1 is studied on near-resonant strong-field excitation of potassium atoms using well-characterized shaped femtosecond laser pulses. Figure 2 shows the excitation and ionization scheme of potassium atoms exposed to a transform limited fs-pulse. The pulse resonantly excites the $4p$ state and *simultaneously* ionizes the atom in a two-photon process, addressing a manifold of final states in the ionization continuum. Upon weak-field excitation, a 1 + 2 REMPI (resonance enhanced multi-photon ionization) process is triggered giving rise to a single peak in the photoelectron spectrum as shown in figure 2(a). The kinetic energy of the peak is given by $3\hbar\omega_0 - \text{IP}$, where $\hbar\omega_0$ is the photon energy and IP is the ionization potential, and—assuming a flat continuum—the width is determined by the spectral width of the ultrashort laser pulse. Since the interaction is perturbative, the ground state population remains essentially unaltered and the total population transfer to the continuum states is negligibly small. In the strong-field regime, however, Rabi cycling (indicated by the bilateral photon arrow in figure 2(b)) within the resonant two-level system $4s$ – $4p$ causes a splitting of the photoelectron signal into the Autler–Townes (AT) doublet [35]. A description in the framework of dressed atomic states, i.e. the eigenstates of the total system comprising the two-level system and the excitation field (faded in figure 2(b)), delivers an elucidative picture of this scenario: in the presence of an intense electric field $E(t)$ the dressed state eigenenergies (bold black lines in figure 2(b)) repel each other resulting in an energy splitting of $\hbar\Omega(t) = \mu E(t)$, with the Rabi frequency $\Omega(t)$ and μ being the electric dipole moment of the $4p \leftarrow 4s$ transition. The ionization field maps this splitting into the photoelectron spectrum and, thus, opens up two different channels for the population transfer to the continuum. In this picture, the key to the control

of the branching ratio between the two channels is readily identified: selective population of the lower (upper) dressed state selectively steers the population towards the low (high) energetic target channel. The energy splitting between the target channels is controlled by the pulse intensity providing tunability among the target states. However, it was shown that there is no dressed state control with the so-called *real-valued* pulses [36], i.e. pulses characterized by an envelope with constant temporal phase (except for π -jumps). While this special class of pulses can be employed to extend weak-field control schemes into the strong-field regime [37], it always produces a purely imaginary excited state amplitude c_{4p} which entails a symmetric AT doublet [36, 38]. Therefore, so-called *complex-valued* pulses, i.e. pulses characterized by an envelope with temporally varying phase, have to be employed in order to make use of new strong-field control mechanisms. There are two basic approaches to realize a temporally varying phase, since the variation can either be discrete, as in the case of pulse sequences, or continuous, which is characteristic for chirped pulses. In our experiments, we pursue both of these complementary approaches to exert control on the dressed state populations by utilizing prototypes of the corresponding pulse shapes, as described in the following section. A detailed discussion of the physical mechanisms behind any of these approaches will be given in section 4.1.1.

3. Experimental details

The experimental strategy is depicted in figure 3. An intense 790 nm, $\Delta t = 30$ fs FWHM (full width at half maximum) input pulse provided by an amplified 1 kHz Ti:sapphire laser system is phase modulated in frequency domain by a home-built pulse shaper [39]. In order to realize the two approaches mentioned above, the spectral phase modulation function applied to the liquid crystal spatial light modulator (LC-SLM) [1, 40] is given by a linear combination of a sine function (periodic term) and a quadratic function (polynomial term):

$$\varphi(\omega) = A \sin[(\omega - \omega_{\text{ref}})T + \phi] + \varphi_2(\omega - \omega_{\text{ref}})^2. \quad (1)$$

The origin ω_{ref} of the modulation function is set close to the laser central frequency ω_0 . Application to the input pulse $\tilde{E}_{\text{in}}^+(\omega)$ yields the modulated electric field in the frequency domain

$$\tilde{E}_{\text{mod}}^+(\omega) = \tilde{E}_{\text{in}}^+(\omega) e^{-i\varphi(\omega)}. \quad (2)$$

This pulse parameterization includes two special cases: by setting $\varphi_2 = 0$ fs² sinusoidal phase modulation is obtained which, in general, produces a multipulse sequence in time domain with subpulses separated by T and discrete temporal phase jumps between adjacent subpulses determined by T and ϕ [37, 41–46]. Two examples of a multipulse sequence can be found in figure 3 (lower layer) and figure 5(a), respectively. On the other hand, choosing $A = 0$ (or $T = 0$ fs) reduces the modulation function to a parabola which, in time domain, results in a linearly chirped pulse, i.e. a temporally broadened field amplitude with lowered peak intensity and a continuous parabolic temporal phase (cf figures 3 and 5(b)). Hence, the combined modulation defined in (1) provides prototypes of

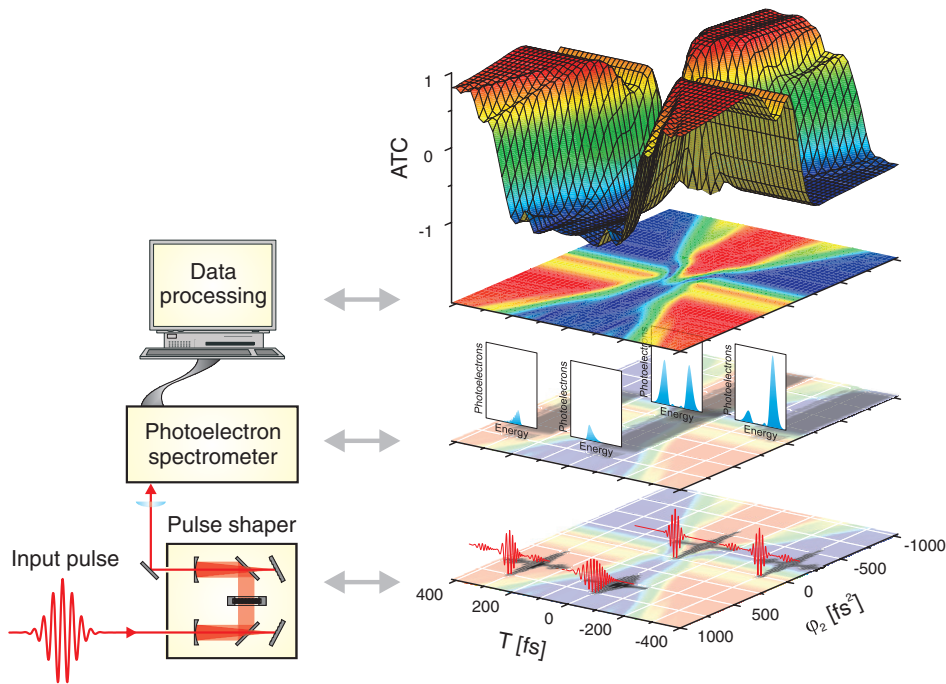


Figure 3. Experimental strategy. Intense 30 fs FWHM input pulses are phase modulated in frequency domain by a Fourier transform pulse shaper. The applied phase modulation function reads $\varphi(\omega) = A \sin[(\omega - \omega_{\text{ref}})T + \phi] + \varphi_2(\omega - \omega_{\text{ref}})^2$ providing pulse sequences (sinusoidal modulation) and linearly chirped pulses (second-order polynomial modulation) as two special cases. The variation of one of the different sine parameters A , T and ϕ versus the chirp parameter φ_2 defines two-dimensional parameter spaces within the search space, one of which is exemplified in the lower layer. Measuring energy resolved photoelectron spectra for a set of parameter combinations (middle layer) and determining the Autler–Townes contrast ATC for each spectrum yields two-dimensional SPODS strong-field control landscapes, as represented in the upper layer. Positive (negative) ATC values correspond to a predominant population of the upper (lower) dressed state in favour of an overall population transfer to the upper (lower) ionic target channel.

complex-valued pulses with either discrete or continuously varying temporal phases and, moreover, allows for a large variety of complex shaped pulses with special features of both types of modulation. Particular cases of a sequence of chirped pulses are displayed in figures 3 and 8. A similar approach to reduce the search space complexity was reported by Bartelt *et al* [30]. In this publication, the authors applied a sinusoidal phase modulation function with the argument being a third-order polynomial in order to interpret results obtained from an optimization of the multi-photon ionization of NaK in the weak-field regime.

An analytic expression of the temporal electric field resulting from (1) can be derived along the lines of [40, 46]

$$E_{\text{mod}}^+(t) = \sum_{n=-\infty}^{\infty} J_n(A) \mathcal{E}_{\text{chirp}}^+(t + nT) e^{in(\Delta\omega T + \phi)} e^{i\omega_0 t}. \quad (3)$$

Herein, J_n is the Bessel function of the first kind and n th order and $\Delta\omega = \omega_0 - \omega_{\text{ref}}$ is the difference between the laser central frequency and the origin of the phase modulation function. For interpulse separations T large compared to the temporal FWHM of the chirped input pulse envelope $\mathcal{E}_{\text{chirp}}^+(t)$ [40]

$$\Delta t_{\text{chirp}} = \sqrt{\Delta t^2 + \left(8 \ln 2 \frac{\varphi_2}{\Delta t}\right)^2}, \quad (4)$$

equation (3) describes a sequence of pulses. The subpulses are the scaled replica of the chirped input pulse. In order to

realize the temporal pulse shape (3) experimentally, we first *in situ* compensate residual spectral phases of the input pulse by adaptively optimizing multi-photon ionization of ground-state xenon atoms in the interaction region of our photoelectron spectrometer (see below). The inverse phase is then applied to the LC-SLM to assure a transform-limited pulse. Complex-valued pulses, generated upon application of the spectral phase (1) in addition, are characterized by spectrogram-based methods [48] confirming the temporal pulse shape as described in (3).

The pulse parameterization (1) represents a natural way to address two distinct classes of pulses: as explicated above, the combined modulation yields either pulses with a discrete (discontinuous) temporal phase, in which the phase discontinuities are controlled by the sine parameters A , T and ϕ , or pulses with a continuous temporal phase controlled by the chirp parameter φ_2 *inter alia*. In general, the control space may be decomposed into a subset of pulses which have a continuous temporal phase and its complement comprising all pulses with a discontinuous phase. In this spirit, the sine parameters and the chirp parameter are *complementary* from a theoretical point of view. A combination of either sine parameter with the chirp parameter hence defines two-dimensional parameter spaces with both dimensions projecting into complementary regions of the control space. Each point of these parameter spaces corresponds to a certain pulse shape characterized either by phase jumps or continuous phase variations, or a combination

of both. This is exemplified in the lower layer of figure 3 for the parameter combination $\{(T, \varphi_2)\}$ spanning a Cartesian coordinate plane. Both parameters are varied within ranges which are feasible for our experimental setup. Restrictions are mainly related to the sine frequency T , due to the finite resolution of the LC-SLM, and the chirp φ_2 which determines the number of jumps in the spectral phase due to phase wrapping. The shaped laser pulses are attenuated to a pulse energy of 0.2–0.5 μJ and focused by a 300 mm lens into a vacuum chamber. The focal conditions correspond to a pulse intensity of 10^{11} – 10^{12} W cm^{-2} . In the chamber, the laser perpendicularly intersects a potassium atomic beam from an adjacent oven chamber. The oven has an exiting nozzle of 200 μm diameter and is operated at 350 $^\circ\text{C}$. Photoelectrons released by the laser–atom interaction are measured by a magnetic bottle time-of-flight spectrometer [49] with an energy resolution of 15 meV at a kinetic energy of 0.5 eV. Calibration of the spectrometer is performed by photoionizing potassium and xenon ground-state atoms using nanosecond lasers with wavelengths of 532 nm, 540 nm and 570 nm, respectively. Kinetic energy resolved photoelectron spectra measured upon femtosecond laser excitation are indicated in the middle layer of figure 3. Finally, the recorded AT doublets are processed by calculating the Autler–Townes contrast

$$\text{ATC} = \frac{F - S}{F + S}, \quad (5)$$

where F and S denote the integrated signal of the fast and slow photoelectrons, respectively. Since the ATC is a measure of the asymmetry of the AT doublet, i.e. the branching ratio of the two ionic target channels, this scalar fitness value gives information about the dressed state populations during the interaction process: an ATC value of -1 corresponds to the selective population of the lower dressed state and vice versa. Therefore, a two-dimensional SPODS strong-field control landscape (SFCL) like the generic one as shown in the upper layer of figure 3 is obtained by plotting the ATC as a function of the corresponding pulse parameters.

The generic SFCL shown in figure 3 is obtained by simulating the photoionization of a resonant two-level atom excited by a 30 fs Gaussian input pulse, shaped according to (1). Our experiments, however, differ from this ideal situation, since the central frequency of our laser spectrum is slightly red-shifted with respect to the potassium $4p \leftarrow 4s$ resonance. In addition, the $4p$ state splits up into the two fine structure components $4p_{1/2}$ (770, 1 nm) and $4p_{3/2}$ (766, 7 nm). In order to match the experimental conditions, we therefore account for the off-resonant excitation of a three-level system in our simulations. A detailed description of the theoretical and numerical treatment is given, for example, in [36, 46, 47].

4. Results and discussion

In this section, we present our experimental results and discuss the findings with regard to physical mechanisms which underlie the different SPODS realizations. First, two SFCLs for the parameter spaces $\{(T, \varphi_2)\}$ and $\{(\phi, \varphi_2)\}$ are shown in section 4.1. Since T and ϕ are the relevant parameters to control the temporal phase jumps in a pulse sequence from

sinusoidal phase modulation [46], these SFCLs are best-suited to analyse the physics behind the SPODS control process. In section 4.2, we report on an evolutionary optimization of SPODS on the parameter space $\{(A, \varphi_2)\}$. The preceding measurement of the control topology enabled us to keep track of the evolution on the surface of the SFCL. The recorded control trajectories (CTs) are visualized and discussed.

4.1. Strong-field control landscapes of SPODS mechanisms

The first parameter space under study is defined by the sine frequency and the chirp parameter: $\{(T, \varphi_2)\}$. This parameter space is especially suited to study the effect of variable phase jumps, continuous phase variations and combinations of both. From (3) it can be seen that for $\Delta\omega \neq 0 \text{ fs}^{-1}$ the delay parameter T directly controls the temporal phase jumps from sinusoidal phase modulation. A detailed discussion of the effect of the delay parameter on the electric field can be found in [46]. Moreover, the choice $T = 0$ fs cancels out the periodic term in (1) allowing for purely chirped pulses on the $T = 0$ fs axis. Figure 4(a) shows the measured SFCL of this two-dimensional parameter space for the fixed parameters $A = 0.25$ and $\phi = \pi/2$. The choice of ϕ effectively leads to a cosine modulation function which is symmetric with respect to the sign of T . This symmetry is reflected by the observed symmetry of the landscape with respect to the φ_2 -axis, confirming high stability of the experimental setup throughout the measurement. A comparison with the simulation result (yellow-shaded inset) which is based on a phase-shaped Gaussian input pulse of 30 fs initial FWHM shows a good agreement. The successful reproduction of experimental results under idealized numerical conditions underscores the reliability of the employed pulse-shaping techniques. Furthermore, this agreement demonstrates the feasibility of open loop strong-field control schemes using specifically designed shaped laser pulses. A top view (contour plot) serves to identify prominent points within the landscape.

At the origin (0 fs, 0 fs^2) the unmodulated pulse produces an almost vanishing ATC, exerting only marginal control on the dressed state populations (cf white 0-stamp in figure 4(a)). The negative sign results from a small red-shift of our laser spectrum with respect to the potassium $4p \leftarrow 4s$ resonance. However, following the T -axis to the points (± 140 fs, 0 fs^2) (cf white PL-stamp in figure 4(a)) delivers pronounced minima with an ATC of -0.8 which indicates a lower dressed state population of about 90%. Here, selective population of the lower dressed state is achieved via pure sinusoidal phase modulation, i.e. pulse sequences with appropriately adjusted temporal phase jumps. Following the φ_2 -axis to the point (0 fs, 800 fs^2) (cf white RAP-stamp in figure 4(a)) leads to the same result. At this point, however, SPODS is realized via a single up-chirped pulse, i.e. continuous variation of the temporal phase. By changing the sign of the chirp parameter this picture is inverted. The down-chirped pulse at (0 fs, -800 fs^2) (cf black RAP-stamp in figure 4(a)) achieves an ATC of $+0.8$, now indicating a population of the *upper* dressed by about 90%. Thus, a change of sign

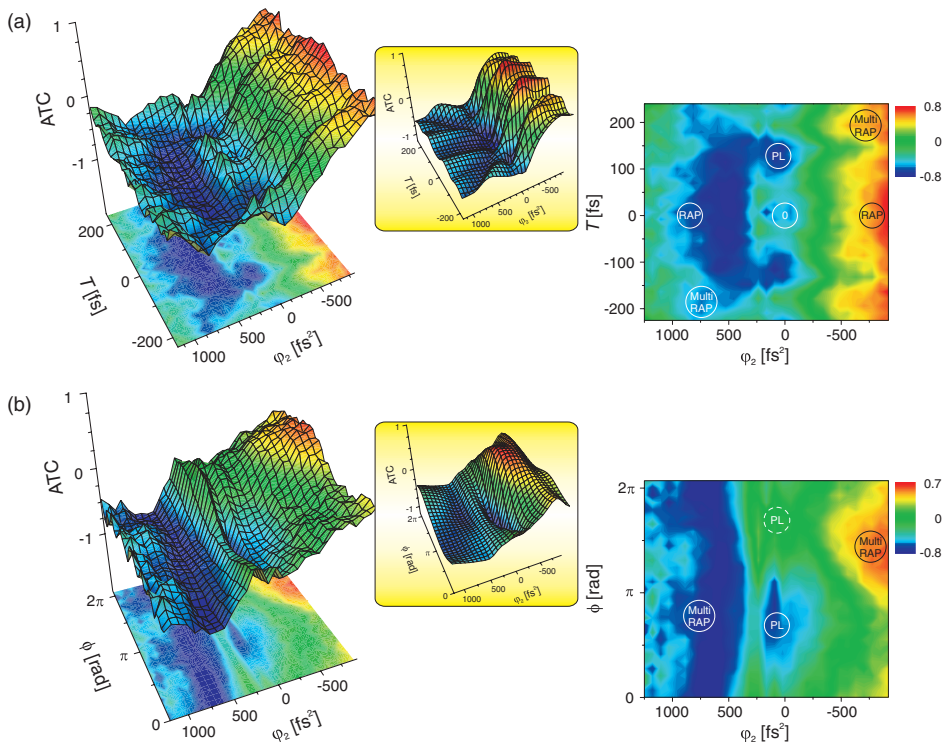


Figure 4. SPODS strong-field control landscapes measured for two-dimensional parameter spaces within the search space. (a) SFCL obtained by the variation of the delay parameter T versus the chirp φ_2 . A comparison with the simulation result (yellow-shaded inset) shows a good agreement. In the contour plot (right), prominent points are attributed to different physical mechanisms: pulse sequences provide a realization of SPODS via photon locking, whereas chirped pulses utilize rapid adiabatic passage to achieve the same result. At diagonal points a combined mechanism termed Multi-RAP is at play (see text). (b) Variation of the phase parameter ϕ versus the chirp yields another SFCL, also being in accordance with the simulation result. Since this parameter space comprises no purely chirped pulses only PL shows up as an elementary SPODS mechanism in the contour plot. However, for large values of φ_2 , the Multi-RAP mechanism is observed as well leading to an efficient realization of SPODS.

of the chirp parameter enables an *efficient* switching among the dressed state populations. Off-axis points yield further realizations of SPODS with both types of modulations being operative simultaneously. This is exemplified by the points $(-200 \text{ fs}, 750 \text{ fs}^2)$ (cf white Multi-RAP-stamp in figure 4(a)), where a predominant population of the lower dressed state is observed, and $(200 \text{ fs}, -750 \text{ fs}^2)$ (cf black Multi-RAP-stamp in figure 4(a)), where the upper dressed state is selected.

Another combination of the sine and chirp parameters is explored by measuring the SFCL of the parameter space $\{(\phi, \varphi_2)\}$, while keeping $A = 0.25$ and $T = 120 \text{ fs}$ fixed. Since ϕ directly controls the temporal phase jumps of a pulse sequence resulting from sinusoidal phase modulation, variation of this parameter should provide a significant degree of control on the dressed state populations. The experimental result is shown in figure 4(b) together with the simulated SFCL, which again reproduces the measurement very well. In fact, for small values of φ_2 , the SFCL shows a pronounced modulation along the φ_2 -axis as ϕ increases from 0 to 2π . The distinct minimum in the vicinity of $(3\pi/4, 0 \text{ fs}^2)$ (cf white PL-stamp in figure 4(b)) is an indicator for the selective population of the lower dressed state. Again, the detuning of our laser spectrum shifts the ATC towards negative values which penalizes the population of the upper dressed state leading to

a less pronounced maximum close to the point $(7\pi/4, 0 \text{ fs}^2)$ (cf dashed white PL-stamp in figure 4(b)). For large values of $|\varphi_2|$, however, ϕ is no longer an active control parameter and another mechanism takes over which makes use of the chirp in addition. Prominent points which demonstrate the realization of SPODS via a combined effect of both modulation types are $(3\pi/4, 750 \text{ fs}^2)$ (cf white Multi-RAP-stamp in figure 4(b)), where the lower dressed state is populated selectively, and $(3\pi/2, -750 \text{ fs}^2)$ (cf black Multi-RAP-stamp in figure 4(b)), where a predominant population of the upper dressed state is observed.

The above presented SFCLs of both the parameter space $\{(T, \varphi_2)\}$ and $\{(\phi, \varphi_2)\}$ clearly exhibit gentle slopes leading to optimal as well as suboptimal local extrema. In addition, our observations highlight that there are various ways to exert control on the dressed state populations with *complex-valued* pulse shapes showing that complementary approaches based on entirely different pulse shapes result in the same degree of attainable control, i.e. all roads lead to Rome. The finding that different pulses achieve the same control objective was recently discussed by Rabitz and co-workers [31, 50]. The authors investigated the level sets of a quantum control landscape, i.e. subsets of pulses which lead to the same value of the control observable, concluding that the constituents of

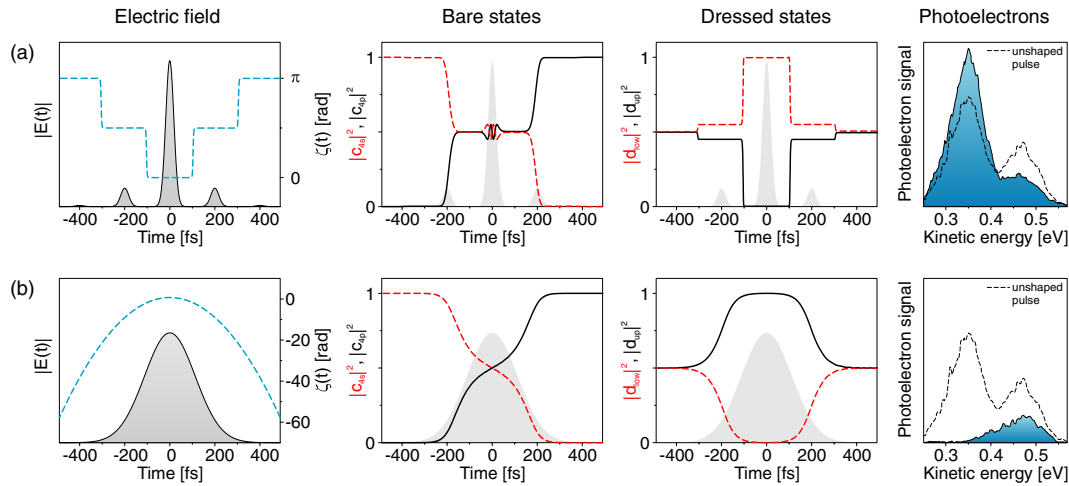


Figure 5. Two different realizations of SPODS based on complementary physical mechanisms. Shown is the simulated excitation/ionization of a two-level atom with intense resonant phase-modulated laser pulses. (a) Sinusoidal modulation with $A = 0.25$, $T = 200$ fs and $\phi = -\pi/2$ delivers a pulse sequence with discrete phase jumps of $\pm\pi/2$. The first prepulse prepares a coherent superposition of the two bare states which is locked during the main pulse due to the phase jump of $-\pi/2$. In the dressed state picture, photon locking leads to quasi-instantaneous selective population of the lower dressed state, indicated by the predominant production of slow photoelectrons. (b) Quadratic modulation with $\varphi_2 = -1000$ fs² yields a single pulse with a continuous parabolic phase. This pulse inverts the bare state populations via rapid adiabatic passage and transiently realizes selective population of the upper dressed state during its most intense part. Since most of the photoelectrons are produced within this time window, only the high energy component of the AT doublet is observed.

such level sets may be vastly different and, consequently, will utilize different control mechanisms to achieve the objective.

We now turn to the discussion of the physical mechanisms behind the different realizations of SPODS. To this end, we first discuss two elementary mechanisms of strong-field control followed by the discussion of a composite mechanism which arises from an interplay of the elementary mechanisms.

4.1.1. Photon locking and rapid adiabatic passage.

In order to elucidate the physics behind the different SPODS realizations described above with greatest clarity, we discuss the photoionization process by means of a two-level atom irradiated by a resonant phase-shaped Gaussian input pulse (30 fs initial FWHM). A detailed discussion including the Bloch vector descriptions of the scenarios described in the following is given in [36, 46]. Figure 5 shows different aspects of the excitation process for (a) a pulse sequence and (b) a chirped pulse. The pulse sequence in the top row is generated by sinusoidal modulation with $A = 0.25$, $T = 200$ fs and $\phi = -\pi/2$. The electric field exhibits discrete temporal phase jumps of $\pm\pi/2$ between adjacent subpulses and thus meets the condition of a *complex-valued* pulse shape. We discuss the interaction with the shaped laser field in a spatiotemporal picture similar to [51]. The first prepulse prepares a superposition state of maximum coherence, i.e. equal population $|c_{4s}|^2 = |c_{4p}|^2 = 0.5$ of the two bare states, and hence induces an electric dipole moment oscillating at the resonance frequency (cf figure 6(a)). In analogy to a classical *resonantly* driven system, the induced dipole moment $\vec{\mu}$ follows the driving field oscillation with a phase shift of $\pi/2$, allowing for an optimal energy transfer to the atom. The subsequent phase jump of $-\pi/2$ at $t = -100$ fs between the first prepulse and the main pulse shifts the field oscillation

in phase with the dipole moment so that further energy transfer is precluded. As a result, the bare state populations are locked during the main pulse which is analog to spin locking known from nuclear magnetic resonance [52]. The process considered here was termed photon locking (PL) [53–55], initially reported on atomic and molecular excitation using *narrow* bandwidth laser radiation. While the bare state populations are frozen due to the phase jump, a dramatic effect is observed in the dressed state picture: since the amplitude of the dipole oscillation is largest at maximum coherence of the bare states and, moreover, the dipole moment is oriented *parallel* to the electric field throughout the main pulse (the right panel of figure 6(a)), the energy of the total system $-\vec{\mu} \cdot \vec{E}$ is minimized. This implies selective population of the *lower* dressed state by the main pulse as observed in figure 5(a). Due to the second-order nature of the ionization step, the major part of the photoelectrons is produced during the most intense main pulse. Hence, the ionization field essentially maps the lower dressed state into the photoelectron spectrum so that only the low-energy AT component shows up. Selective population of the upper dressed state via PL is shown in figure 6(b): a phase jump of $+\pi/2$ —provided by the choice of $\phi = +\pi/2$ —will result in the dipole moment oscillation phase-shifted by π with respect to the electric field of the main pulse. Thus, both vectors are oriented *antiparallel* and the energy of the total system is maximized, corresponding to the selective population of the *upper* dressed state [46]. Illustrative animations of SPODS realized via PL are available at stacks.iop.org/JPhysB/41/074007.

The photoelectron spectra shown in figure 5(a) are measured upon near-resonant excitation of potassium with an unmodulated 30 fs pulse (dashed spectrum) and after the application of an appropriate sinusoidal phase mask (shaded

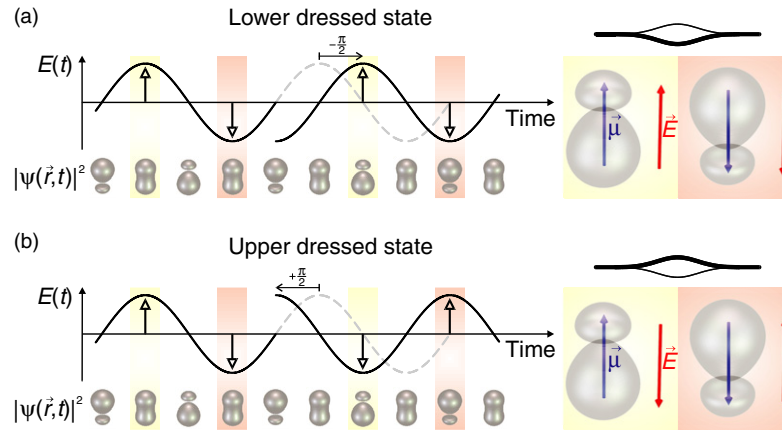


Figure 6. SPODS via photon locking discussed in a spatiotemporal picture. Shown are the carrier oscillation of the driving electric field $\vec{E}(t)$ as compared to the induced oscillation of the atomic wavefunction $|\psi(\vec{r}, t)|^2$ at maximum coherence. The latter gives rise to an oscillating electric dipole moment $\vec{\mu}$, initially following the driving force with a phase shift of $\pi/2$. (a) A carrier phase jump of $-\pi/2$ by suitable *spectral* phase modulation shifts the electric field *in phase* with the dipole moment such that subsequently both vectors oscillate parallel. In this configuration the populations are *locked* and, hence, the dipole oscillation remains unaltered. (b) The same applies to a phase shift of $+\pi/2$ which leads to the antiparallel oscillation of \vec{E} and $\vec{\mu}$. Since the amplitude of the dipole oscillation is largest at a state of maximum coherence, the parallel (antiparallel) configuration minimizes (maximizes) the energy $-\vec{\mu} \cdot \vec{E}$ of the interacting system which is equivalent to selective population of the lower (upper) dressed state.

spectrum). As was discussed in the previous section, even the unmodulated pulse slightly favours the lower dressed state, giving rise to the observed slight asymmetry of the AT doublet. However, excitation by the sinusoidally modulated pulse promotes the generation of slow electrons significantly, while suppressing the fast electrons. Note that the photoelectron yield, i.e. the integrated photoelectron intensity, is essentially unaffected by application of the sinusoidal phase modulation, since for small values of A the peak intensity of the main pulse is only negligibly decreased compared to that of the unmodulated pulse. In view of the overall process involving resonant excitation and nonlinear ionization, this indicates high efficiency of the population transfer to the target states achieved by SPODS via PL.

The dynamics induced by a continuously varying phase in the photoionization process is illustrated in figure 5(b). The electric field depicted here results from quadratic phase modulation with $\varphi_2 = -1000 \text{ fs}^2$ (down-chirp) which yields a temporally broadened field amplitude with a quadratic phase likewise matching the condition of a *complex-valued* pulse shape. The mechanism which underlies the SPODS realization in this case is rapid adiabatic passage (RAP) [56]. Provided the adiabatic condition [36, 56, 57] is fulfilled, i.e. the pulse intensity is sufficiently high and/or the sweep of the instantaneous frequency introduced by the nonlinear phase is sufficiently rapid, the bare state populations adiabatically follow the electric field to end up in an inversion of the two-level atom. A similar behaviour is obtained in the dressed state picture. As the optical phase varies, the populations continuously evolve from the initial equal population into the selective population of the upper dressed state during the most intense part of the pulse. Again, since ionization occurs mainly within this time window, the resulting photoelectron signal is dominated by the fast electron contribution, i.e. only the high

energy AT component shows up. The exclusive production of slow photoelectrons due to selective population of the lower dressed state is obtained by changing the sign of the chirp parameter to $\varphi_2 = +1000 \text{ fs}^2$ (up-chirp) which is not shown here [36].

An AT doublet measured upon near-resonant down-chirped excitation of potassium is shown in figure 5(b) (shaded spectrum). In fact, the production of slow electrons is completely suppressed indicating supreme selectivity of the population transfer to the ionic target states achieved by SPODS via RAP. However, due to the lowered peak intensity of the chirped pulse, the amount of photoelectrons produced by the two-photon ionization process is significantly reduced with respect to the unmodulated pulse and, consequently, with respect to the results obtained via PL.

While RAP is an adiabatic process based on a smooth guidance of the system, PL is characterized by a strongly non-adiabatic time evolution with rather abrupt changes of the system which occur quasi-instantaneously, i.e. within one optical cycle. Experimentally, the complementarity between PL and RAP manifests itself in the overall population transfer efficiency. In addition, this complementary character is reflected in the robustness of the two mechanisms with respect to experimental conditions. In strong-field control, the robustness of nonlinear processes with respect to variations of the pulse intensity is of special importance. In order to illustrate this aspect, figure 7 presents measured photoelectron spectra generated via PL (upper row) and RAP (lower row), respectively, which highlight the interplay between phase and intensity. For the results shown in the upper row, a sinusoidal phase modulation with $A = 0.25$ and $T = 120 \text{ fs}$ was applied. The blue-shaded photoelectron spectra (solid line) correspond to a sine phase of $\phi = 1.2 \text{ rad}$, whereas a sine phase of $\phi = 5.1 \text{ rad}$ was set to obtain the green-shaded spectra (dashed

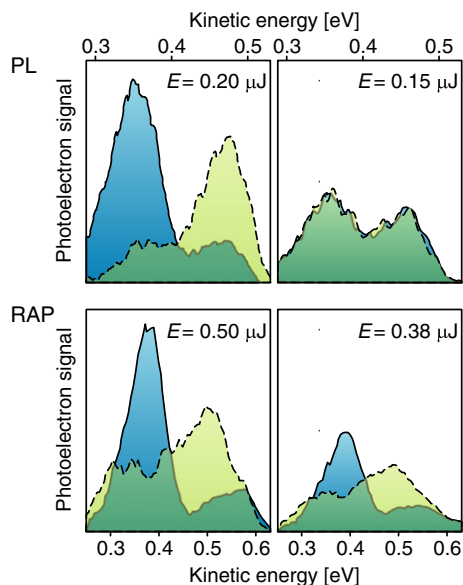


Figure 7. Measured AT doublets produced via photon locking (top row) and rapid adiabatic passage (bottom row). For the top row results, sinusoidal phase functions with $A = 0.25$, $T = 120$ fs and $\phi = 1.2$ rad (solid, blue) or $\phi = 5.1$ rad (dashed, green) were applied, respectively. The bottom row results were obtained by quadratic modulation with $\varphi_2 = 350$ fs² (solid, blue) and $\varphi_2 = -200$ fs² (dashed, green). Illustrated is the robustness of the two SPODS mechanisms with respect to the variations of the intensity. PL is inherently sensitive to the pulse intensity since the full dressed state control is only provided if the system is initially prepared in a superposition state of maximum coherence (top left). By suitable choice of the intensity, however, phase control is inhibited (top right). RAP is extremely robust with respect to the intensity. The variation of the intensity therefore leaves the shape of the measured photoelectron spectra basically unaffected (bottom row).

line). A pulse energy of $0.20 \mu\text{J}$ yields highly asymmetric AT doublets (left plot), reflecting selective population of a single dressed state via PL. At this intensity the phase provides a substantial degree of controllability. However, controllability by the phase is inhibited if we decrease the pulse energy by 25% ($0.15 \mu\text{J}$), as shown in the right plot. At this intensity, nearly symmetric AT doublets are produced for all phases ϕ . In fact, controllability by the phase can be turned on and off by the intensity of the pulse [38]. The reason why PL is affected by the intensity lies in the initial preparation of a superposition state within the two-level system. A maximum degree of controllability is provided if the first prepulse achieves a state of maximum coherence. Ground state or inverted atoms, in contrast, completely preclude controllability.

In contrast, the RAP mechanism is basically unaffected by the pulse intensity. This is illustrated in the lower row, where the photoelectron spectra were measured upon quadratic modulation with $\varphi_2 = 350$ fs² (solid line, blue-shaded) and $\varphi_2 = -200$ fs² (dashed line, green-shaded). AT doublets obtained with a pulse energy of $0.50 \mu\text{J}$ (left) again show a pronounced asymmetry due to the realization of SPODS via RAP. Unlike the case of PL, this asymmetry is maintained as we reduce the intensity by 25% ($0.38 \mu\text{J}$, right). In accordance with the adiabatic condition, for a given frequency sweep, i.e.

chirp parameter φ_2 , the performance of RAP becomes more and more stable with increasing intensity.

In summary, PL and RAP are two complementary approaches to realize SPODS either non-adiabatically or adiabatically. In a multistep process, PL provides a high overall population transfer efficiency but the selectivity/controllability of the population transfer strongly depends on the subpulse intensity. RAP, on the other hand, provides high selectivity/controllability as well as an enormous robustness with respect to experimental parameters such as pulse intensity and detuning. The total yield in a multistep process, however, is significantly reduced in comparison to PL if the fluence is kept constant. These observations support the theoretical concept of complementary control parameters (see section 3) from the experimental perspective.

While both mechanisms were initially observed in experiments involving continuous wave excitation, new aspects come into play when ultrashort laser pulses are applied: switching of population transfer on an ultrashort time scale will outperform decoherence processes which is crucial for quantum information processing as well as control of chemical reactions. Dressed state energy shifts of the order of 100 meV [5] obtained by the high peak intensity of femtosecond laser pulses are the essential prerequisite to applications in chemistry [5, 58] since this is the typical energy separation of different target states in molecules. The potential of shaped femtosecond laser pulses for ultrafast switching is examined in the following section where we discuss the combination of PL and RAP. An example of multiple quantum logical operations on a sub-picosecond time scale is presented.

4.1.2. Multi-RAP. While the two SPODS mechanisms PL and RAP have been discussed in earlier work (see above), the effect of the combined modulation (1) on the resonant excitation of a two-level atom has not been considered yet. In this section, resonant excitation and ionization of a two-level atom by a 30 fs Gaussian input pulse which is phase-shaped by a modulation function of the form (1) with $A = 0.25$, $\phi = -\pi/2$ and $\varphi_2 = -1000$ fs² is discussed. The resulting temporal electric field is generally a sequence of linearly chirped pulses separated by the sine frequency T and chirped according to φ_2 . In the following, we will distinguish two marginal cases representing two distinct physical mechanisms, both of which are illustrated in figure 8. In figure 8(a), the sine frequency is set to $T = 80$ fs, which is below the temporal FWHM $\Delta t_{\text{chirp}} = 187$ fs of the chirped pulse obtained from (4). Consequently, the subpulses overlap in time resulting in a global parabolic phase without phase jumps. Note that the shoulders in the envelope at $t = \pm 120$ fs and $t = \pm 280$ fs do not reflect the actual subpulse separation of $T = 80$ fs. Instead, these structures arise from optical interferences within the overlapping subpulses. The electric field thus acts as one amplitude modulated down-chirped pulse inducing bare and dressed state dynamics which are very similar to those of the conventional RAP (cf figure 5(b)). Due to the down-chirp, the upper dressed state is selectively populated during the most intense part of the pulse so that primarily fast photoelectrons are produced. The substructure of the (generic)

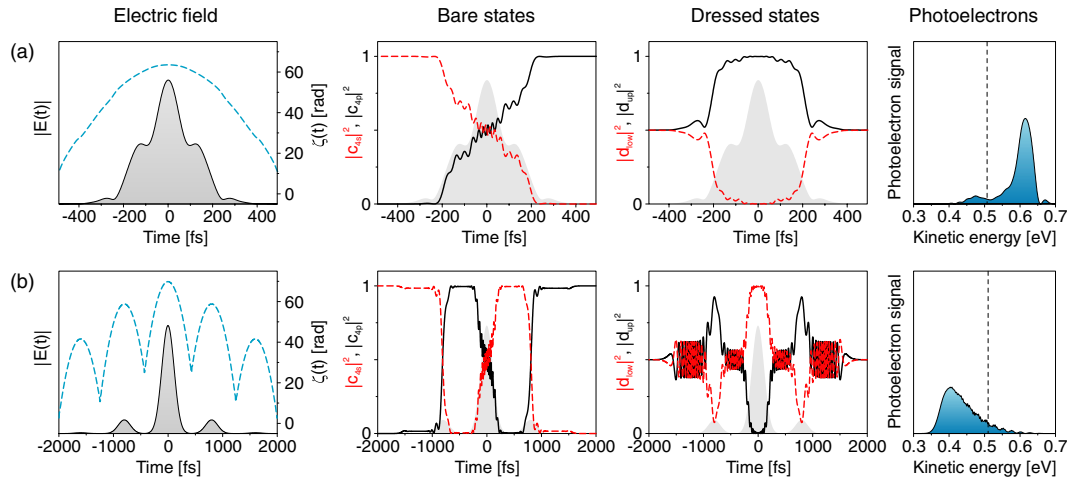


Figure 8. Multi-RAP mechanism discussed on resonant excitation/ionization of a two-level atom by a sequence of chirped pulses resulting from the combined modulation (1). (a) For interpulse separations smaller than the width of the subpulses, a single amplitude modulated pulse with a global (nearly) parabolic phase is formed. Such a pulse sequence acts like a single chirped pulse on the atom inducing conventional RAP-type dynamics in the bare states, the dressed states and the released photoelectrons. (b) In the case of fully separated subpulses every pulse with sufficiently high energy performs an individual RAP, thereby inverting the bare states or inducing a complete population return to the ground state. This leads to multiple sequential realizations of SPODS with alternating population of the upper and the lower dressed state. The intensity distribution among the subpulses determines which dressed state is mapped into the continuum. The photoelectron spectra (right panels) show that in the Multi-RAP scenario the pulse separation is also an active control parameter.

AT doublet results from interference of free electron wave packets [46, 59, 60] launched by the different subpulses. This marginal case where SPODS is realized via a RAP-type process even in the presence of a multipulse sequence is observed in the SFCLs as shown in figure 4 for large values of the chirp parameter (cf Multi-RAP-stamps in figures 4(a) and (b)).

This picture changes as the interpulse separation is increased beyond the temporal width of the subpulses. In figure 8(b), the sine frequency is set to $T = 800$ fs in order to separate the subpulses in time. Provided the pulse energy is sufficiently high, every pulse is capable of performing a single RAP. In general, this will result in multiple sequential realizations of RAP which we shortly term Multi-RAP. In our generic example, this condition is fulfilled for all the three central pulses, the first of which already inverts the atom via RAP, favouring the *upper* dressed state in virtue of the down-chirp. The main pulse encounters the atom in the excited $4p$ state and, hence, induces an inverted RAP that leads to a population return to the $4s$ ground state. In sharp contrast to the conventional RAP (see section 4.1.1), here, the *down*-chirped pulse gives rise to selective population of the *lower* dressed state. From a physical point of view this is rationalized by considering the interaction of an inverted atom with a down-chirped laser pulse upon time reversal: transforming t into $-t$ initializes the atom in the ground state. The time evolution induced by the chirped pulse therefore is conventional RAP and leads to bare state inversion. However, time reversal converts the *down*- into an *up*-chirped pulse, which entails selective population of the lower dressed state shown in figure 8(b) at $t = 0$ fs.

The first postpulse at $t = 800$ fs is simply a time-shifted replica of the first prepulse, likewise finding the atom in

the ground state. Consequently, the induced time evolutions are identical, involving another inversion of the bare states and a transient population of the upper dressed state. The photoelectron spectrum, however, is essentially generated during the intense main pulse. Corresponding to selective population of the lower dressed state within this time window, the AT doublet is characterized by a prevailing contribution of slow electrons. We note that while this marginal case of pure Multi-RAP is not observed in the measured SFCLs (cf figure 4) due to the experimental limitation of the interpulse separations T (cf section 3), very pronounced realizations can be found in the *simulated resonant* SFCL shown in figure 3 in the vicinity of $(T, \varphi_2) \approx (\pm 400 \text{ fs}, \pm 1000 \text{ fs}^2)$. In view of the bare state dynamics, a related process termed piecewise adiabatic passage (PAP) was recently discussed by Shapiro *et al* [61] in the context of merging the fields of coherent control via multiple interfering quantum pathways and adiabatic passage techniques [62].

The Multi-RAP scenario indicates that the application of the combined modulation extends the degree of controllability on the total population transfer. Although in this scenario RAP is the elementary SPODS mechanism at play, the sine parameters can also be used to control the outcome of the ionization process. As discussed above, T determines whether the process is conventional or Multi-RAP which addresses different continuum channels as demonstrated in the examples of figure 8. In addition, the sine amplitude A plays an important role: since A controls the intensity distribution among the subpulses (cf equation (3)), it preselects the pulses of the most efficient overall population transfer and hence determines which dressed state is mapped into the continuum. Therefore, all three parameters act independently on the population transfer controlling its pathway to the target states.

Finally, we note that the Multi-RAP pulse sequence suggests the use of shaped ultrashort light pulses for quantum information processing [63–65]. Full control over the electric field by pulse shaping provides a means to efficiently navigate in the Hilbert space [66] which is at the heart of quantum computation. Moreover, the ultrashort interaction time allows for quantum logical operations at an unprecedented rate to effectively outperform coherence destroying processes.

4.2. Evolution on a strong-field control landscape

The topology of quantum control landscapes as introduced by Rabitz *et al* [17, 18] is of fundamental interest for both optimal control theory and experiment since it determines not only the degree but also the quality of attainable control with respect to a certain control target. Theoretical studies [17, 18] indicate that quantum control landscapes, i.e. mappings of the control space onto specific target spaces, exhibit only extrema which correspond to full control or no control at all. What is more, extrema corresponding to full control are pointed out to be remarkably robust and easily accessible for optimization procedures [18]. However, in experimental realizations of these procedures practical constraints inherently restrict the laboratory search to the lower dimensional search space. In general, the search space control landscape amenable to experimental studies is restricted by inherent constraints such as limited laser bandwidth and intensity, etc, as well as the experimenter’s choice of both the control parameters and their ranges. The experimental landscape is only a section of the quantum control landscape and hence suboptimal local extrema cannot be ruled out. In fact, experimental observations confirm the existence of suboptimal extrema [29] (see figure 4). As a consequence, in general, it is neither guaranteed nor to be expected that an adaptive optimization procedure implemented in the laboratory reaches the global optimum.

The question of whether the optimization algorithms in practice end up at the global optimum or eventually become trapped by suboptimal local solutions may not be answered in general due to the facts that the dimension of the search space is still enormous and absolute product yields are normally not known. However, approaching this question on a lower dimensional parameter space provides a hint on the circumstances encountered under more complex conditions.

To this end, we measured the topology of the remaining two-dimensional parameter space $\{(A, \varphi_2)\}$ while keeping the parameters $T = 120$ fs and $\phi = \pi$ fixed. The variation of A and φ_2 within the ranges $[0, 1.2]$ and $[-510 \text{ fs}^2, 510 \text{ fs}^2]$, respectively, yielded the complex structured SFCL as shown in figure 9. The SFCL exhibits suboptimal as well as optimal extrema underscoring the above statements. Due to the particular choice of parameters, the latter are in fact *local* optimal extrema as compared to the ATC values of 0.8 observed in the experiments presented above (see figure 4). In order to examine the performance of an adaptive optimization procedure on this parameter space, we subsequently applied the same pulse parameterization to an evolutionary optimization algorithm [67, 68], allowing for a

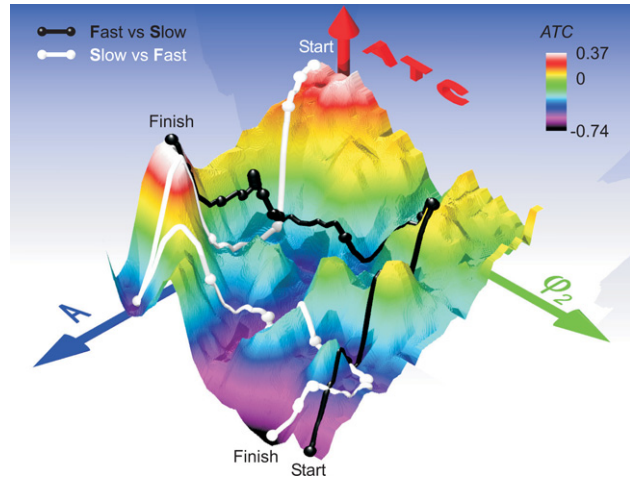


Figure 9. Highly structured SPODS strong-field control landscape measured by the variation of the sine amplitude A versus the chirp φ_2 . The black (white) control trajectory on the top of the landscape shows the evolution of an adaptive optimization procedure for the upper (lower) dressed state. Every sphere indicates the measured mean value of the pulse individual distribution for one generation in the course of the optimization. The black (white) ribbon connects the spheres in chronological order and serves to guide the eye. Despite the existence of suboptimal local extrema, the algorithm was in both runs capable of finding a way to the optimal solution.

variation of A and φ_2 within the ranges of the SFCL. The fitness of the optimization was defined by the ATC which opens up two distinct control objectives described in the following. In the first run, we optimized the upper dressed state population upon maximization of the ATC. The experimental result is illustrated by the black control trajectory (CT) in figure 9. The first generation, i.e. the starting point of the evolution was fixed to the minimum at the front corner of the SFCL. From here, the optimization evolved spreading its individuals all-over the landscape. Black spheres—some of which are hidden behind landscape features—indicate the measured mean values $(\langle A \rangle, \langle \varphi_2 \rangle)$ of the pulse individual distributions corresponding to different generations of the optimization. The black ribbon connecting the spheres in chronological order, i.e. in succession of the generations, serves as a guide to the eye. This representation gives an illustrative picture of the progression of the algorithm on the landscape surface. The progression can roughly be divided into three stages: at the first stage, the algorithm quickly evolved from the bottom of the landscape along the A -axis into the highland of local yet suboptimal maxima. Having reached the highest of these peaks, the algorithm enters the second stage which is characterized by a strong attraction exerted by the two pronounced maxima on the back and on the left-hand side of the landscape. As a result, the algorithm proceeded parallel to the φ_2 -axis to end up at the slope exactly in between the two maxima. The large number of spheres at this point indicates that individuals focus on both maxima in equal measure so that here the algorithm remained undetermined like a donkey between two haystacks. In the end, however, the global maximum on the left-hand side gained the upper hand and the third stage of the optimization is constituted by a steady

ascension of the algorithm until it finally arrived at the summit of the optimal solution.

In the second run, we optimized the population of the lower dressed state by minimizing the ATC (maximization of $-ATC$). This is illustrated by the white CT in figure 9, with the white spheres indicating measured mean values of the individual distributions in the course of the optimization. The first generation was constrained to the pronounced maximum at the back of the SFCL. From this starting point, the algorithm descended along the A -axis into the surrounding valley, aiming towards the isolated minimum beyond the global maximum. However, the algorithm soon realized the suboptimality of this minimum and more and more individuals settled in the lower lying central region of the landscape. Pioneering individuals which already reached the lowlands of the landscape dragged the algorithm along the φ_2 -axis to the low-lying plateau situated in the front of the landscape. From here, the way down to the global minimum was straightforward and the algorithm again ended up at the optimal solution. Animations of both runs, which provide additional insights into the landscape topology as well as the performance of the optimization procedures, can be found at stacks.iop.org/JPhysB/41/074007.

To conclude, adaptive optimizations performed under experimental conditions including noise, such as laser or particle density fluctuations, demonstrate that in low-dimensional cases like the one examined here the algorithm is reliably capable of discovering the optimum. We suspect that these findings may be generalized to larger spaces and more complex situations as well. Our studies show that the set of parameters $\{(A, T, \phi, \varphi_2, I)\}$, where I is the laser intensity, defines a physically motivated parameter space for efficient optimization in resonant strong-field control scenarios.

5. Summary and conclusions

In this paper, we investigate physical mechanisms of resonant strong-field control on the Autler–Townes doublet in the photoelectron spectrum from multi-photon ionization of potassium atoms with intense shaped femtosecond laser pulses. In order to gain insight into the multitude of physical mechanisms involved in coherent control by intense shaped laser pulses, we study the topology of strong-field control landscapes (SFCLs). To this end, physically motivated pulse parameterizations comprising pulse sequences as well as linearly chirped pulses are introduced to map out two-dimensional parameter spaces. The measured SFCLs reveal the topology of these parameter spaces and provide a map of the involved physical mechanisms. Complementary mechanisms such as photon locking (PL) and rapid adiabatic passage (RAP) are realized by a suitable choice of complementary control parameters. A unifying framework for both these control scenarios is provided by selective population of dressed states (SPODS), i.e. PL and RAP turn out to be two sides of the same coin. A new mechanism, which arises when both PL and RAP are at play simultaneously shows up in the SFCLs and is discussed in terms of multiple sequential realizations of RAP (Multi-RAP). Multi-RAP pulses provide a simple example of multiple

quantum logic operations performed within a single shaped pulse on a sub-picosecond time scale. In general, the use of resonant intense shaped pulses is of great promise to quantum information processing since these pulses will allow us to perform arbitrary quantum logic operations at an unprecedented rate implying the potential to outperform decoherence processes.

In order to better understand the physics of adaptive optimization procedures, we experimentally study the performance of such an algorithm to optimize SPODS on a previously measured SFCL. We introduce the concept of control trajectories (CTs) to visualize the evolution of our optimization procedure and discuss CTs measured on the same subset of pulses. Our results show that even in the presence of suboptimal local extrema the algorithm succeeds to find the optimum. Generalizing our findings, we devise a set of adequately chosen robust parameters suitable to study resonant strong-field quantum control scenarios.

Acknowledgment

Financial support by the Deutsche Forschungsgemeinschaft (DFG) is gratefully acknowledged.

References

- [1] Weiner A M 2000 *Rev. Sci. Instrum.* **71** 1929–60
- [2] Brixner T, Pfeifer T, Gerber G, Wollenhaupt M and Baumert T 2005 *Femtosecond Laser Spectroscopy* ed P Hannaford (New York: Springer) chapter 9
- [3] Shapiro M and Brumer P 2003 *Principles of the Quantum Control of Molecular Processes* (New York: Wiley)
- [4] Rice S A and Zhao M 2000 *Optical Control of Molecular Dynamics* (New York: Wiley)
- [5] Wollenhaupt M, Liese D, Präkelt A, Sarpe-Tudoran C and Baumert T 2006 *Chem. Phys. Lett.* **419** 184–90
- [6] Frohnmeyer T, Hofmann M, Strehle M and Baumert T 1999 *Chem. Phys. Lett.* **312** 447–54
- [7] Sussman B J, Townsend D, Ivanov M Y and Stolow A 2006 *Science* **314** 278–81
- [8] Solá I R, Chang B Y, Santamaría J, Malinovsky V S and Krause J L 2000 *Phys. Rev. Lett.* **85** 4241–4
- [9] Gräfe S, Akimov D A, Böhm B, Zheltikov A M, Scully M O, Kiefer W, Engel V and Siebert T 2007 *J. Raman Spectrosc.* **38** 998–1005
- [10] Wollenhaupt M, Präkelt A, Sarpe-Tudoran C, Liese D and Baumert T 2005 *J. Opt. B* **7** 270–6
- [11] Judson R S and Rabitz H 1992 *Phys. Rev. Lett.* **68** 1500–3
- [12] Assion A, Baumert T, Bergt M, Brixner T, Kiefer B, Seyfried V, Strehle M and Gerber G 1998 *Science* **282** 919–23
- [13] Baumert T, Brixner T, Seyfried V, Strehle M and Gerber G 1997 *Appl. Phys. B* **65** 779–82
- [14] Meshulach D, Yelin D and Silberberg Y 1997 *Opt. Commun.* **138** 345–8
- [15] Bardeen C J, Yakolev V V, Wilson K R, Carpenter S D, Weber P M and Warren W S 1997 *Chem. Phys. Lett.* **280** 151–8
- [16] Rabitz H, de Vivie-Riedle R, Motzkus M and Kompa K 2000 *Science* **288** 824–8
- [17] Rabitz H A, Hsieh M M and Rosenthal C M 2004 *Science* **303** 1998–2001
- [18] Rabitz H, Ho T-S, Hsieh M, Kosut R and Demiralp M 2006 *Phys. Rev. A* **74** 012721

- [19] Oron D, Dudovich N and Silberberg Y 2003 *Phys. Rev. Lett.* **90** 213902
- [20] Brixner T, Krampert G, Pfeiffer T, Selle R, Gerber G, Wollenhaupt M, Gräfe O, Horn C, Liese D and Baumert T 2004 *Phys. Rev. Lett.* **92** 208301
- [21] Stapelfeldt H and Seideman T 2003 *Rev. Mod. Phys.* **75** 543–57
- [22] Itatani J, Levesque J, Zeidler D, Niikura H, Pepin H, Kieffer J C, Corkum P B and Villeneuve D M 2004 *Nature* **432** 867–71
- [23] Horn C, Wollenhaupt M, Krug M, Baumert T, de Nalda R and Bañares L 2006 *Phys. Rev. A* **73** 031401
- [24] de Nalda R, Horn C, Wollenhaupt M, Krug M, Bañares L and Baumert T 2007 *J. Raman Spectrosc.* **38** 543–50
- [25] Brixner T, Kiefer B and Gerber G 2001 *Chem. Phys.* **267** 241–6
- [26] Weinacht T C, Bartels R, Backus S, Bucksbaum P H, Pearson B, Geremia J M, Rabitz H, Kapteyn H C and Murnane M M 2001 *Chem. Phys. Lett.* **344** 333–8
- [27] Montgomery M A, Meglen R R and Damrauer N H 2006 *J. Phys. Chem. A* **110** 6391–4
- [28] Montgomery M A, Meglen R R and Damrauer N H 2007 *J. Phys. Chem. A* **111** 5126–9
- [29] Wollenhaupt M, Präkelt A, Sarpe-Tudoran C, Liese D and Baumert T 2005 *J. Mod. Opt.* **52** 2187–95
- [30] Bartelt A F, Feurer T and Wöste L 2005 *Chem. Phys.* **318** 207–16
- [31] Roslund J, Roth M and Rabitz H 2006 *Phys. Rev. A* **74** 043414
- [32] Shane J C, Lozovoy V V and Dantus M 2006 *J. Phys. Chem. A* **110** 11388–91
- [33] Langhojer F, Cardoza D, Baertschy M and Weinach T 2005 *J. Chem. Phys.* **122** 014102
- [34] Cardoza D, Trällero-Herrero C, Langhojer F, Rabitz H and Weinacht T 2005 *J. Chem. Phys.* **122** 124306
- [35] Autler S H and Townes C H 1955 *Phys. Rev.* **100** 703–22
- [36] Wollenhaupt M, Präkelt A, Sarpe-Tudoran C, Liese D and Baumert T 2006 *Appl. Phys. B* **82** 183–8
- [37] Dudovich N, Polack T, Pe'er A and Silberberg Y 2005 *Phys. Rev. Lett.* **94** 083002
- [38] Wollenhaupt M, Assion A, Bazhan O, Horn C, Liese D, Sarpe-Tudoran C, Winter M and Baumert T 2003 *Phys. Rev. A* **68** 015401
- [39] Präkelt A, Wollenhaupt M, Assion A, Horn C, Sarpe-Tudoran C, Winter M and Baumert T 2003 *Rev. Sci. Instrum.* **74** 4950–3
- [40] Wollenhaupt M, Assion A and Baumert T 2007 *Springer Handbook of Lasers and Optics* ed F Träger (New York: Springer) chapter 12
- [41] Weiner A M, Leaird D E, Wiederrecht G P and Nelson K A 1990 *Science* **247** 1317–9
- [42] Dudovich N, Dayan B, Gallagher Faeder S M and Silberberg Y 2001 *Phys. Rev. Lett.* **86** 47–50
- [43] Herek J L, Wohlleben W, Cogdell R, Zeidler D and Motzkus M 2002 *Nature* **417** 533–5
- [44] Lozovoy V V, Pastirk I, Wólłowicz A and Dantus M 2003 *J. Chem. Phys.* **118** 3187–96
- [45] Bartelt A, Lindinger A, Lupulescu C, Vajda Š and Wöste L 2003 *Phys. Chem. Chem. Phys.* **5** 3610–5
- [46] Wollenhaupt M, Präkelt A, Sarpe-Tudoran C, Liese D, Bayer T and Baumert T 2006 *Phys. Rev. A* **73** 063409
- [47] Wollenhaupt M, Bayer T, Krug M, Sarpe-Tudoran C and Baumert T 2007 *J. Phys.: Conf. Ser.* **88** 012053
- [48] Gu X, Akturk S, Shreenath A P, Cao Q and Trebino R 2004 *Opt. Rev.* **11** 141–52
- [49] Kruit P and Read F H 1983 *J. Phys. E: Sci. Instrum.* **16** 313–24
- [50] Rothman A, Ho T-S and Rabitz H 2006 *Phys. Rev. A* **73** 053401
- [51] Kosloff R, Hammerich A D and Tannor D 1992 *Phys. Rev. Lett.* **69** 2172–5
- [52] Hartmann S R and Hahn E L 1962 *Phys. Rev.* **128** 2042–53
- [53] Sleva E T, Xavier I M Jr and Zewail A H 1985 *J. Opt. Soc. Am. B* **3** 483–7
- [54] Bai Y S, Yodh A G and Mossberg T W 1985 *Phys. Rev. Lett.* **55** 1277–80
- [55] Tannor D J, Kosloff R and Bartana A 1999 *Faraday Discuss.* **113** 365–86
- [56] Vitanov N V, Halfmann T, Shore B W and Bergmann K 2001 *Annu. Rev. Phys. Chem.* **52** 763–809
- [57] Baum J, Tycko R and Pines A 1985 *Phys. Rev. A* **32** 3435–47
- [58] Wollenhaupt M and Baumert T 2006 *J. Photochem. Photobiol. A* **180** 248–55
- [59] Wollenhaupt M *et al* 2002 *Phys. Rev. Lett.* **89** 173001
- [60] Winter M, Wollenhaupt M and Baumert T 2006 *Opt. Commun.* **264** 285–92
- [61] Shapiro E A, Milner V, Menzel-Jones C and Shapiro M 2007 *Phys. Rev. Lett.* **99** 033002
- [62] Král P, Thanopoulos I and Shapiro M 2007 *Rev. Mod. Phys.* **79** 53–77
- [63] Tesch C M and de Vivie-Riedle R 2002 *Phys. Rev. Lett.* **89** 157901
- [64] Li X, Wu Y, Steel D, Gammon D, Stievater T H, Katzer D S, Park D, Piermarocchi C and Sham L J 2003 *Science* **301** 809–11
- [65] Stuffer S, Ester P and Zrenner A 2006 *Phys. Rev. Lett.* **96** 037402
- [66] Unanyan R G, Fleischhauer M, Vitanov N V and Bergmann K 2002 *Phys. Rev. A* **66** 042101
- [67] Schwefel H P 1995 *Evolution and Optimum Seeking* (New York: Wiley)
- [68] Bäck T 1996 *Evolutionary Algorithms in Theory and Practice* (New York: Oxford University Press)